Progress In Electromagnetics Research C, Vol. 128, 1–15, 2023

Decoupling Control of Outer Rotor Coreless Bearingless Permanent Magnet Synchronous Generator Based on Online Least Squares Support Vector Machine Inverse System and Internal Model Controllers

Huangqiu Zhu and Liangyu Shen*

Abstract—An outer rotor coreless bearingless permanent magnet synchronous generator (ORC-BPMSG) is a multivariable, nonlinear, and strongly coupled system. In order to realize the precise control of the ORC-BPMSG, a decoupling control strategy based on online least squares support vector machine (OLS-SVM) inverse system and internal model controllers is proposed. Firstly, on the basis of introducing its operation principle, the mathematical model is established. Secondly, on the basis of analyzing its reversibility, a real-time inverse system of ORC-BPMSG is obtained by using OLS-SVM, and it is connected in series with the original system to form a pseudo-linear system, which realizes the linearization and decoupling of the ORC-BPMSG. Thirdly, the internal model controller is designed to perform closed-loop control of the pseudo-linear system. Finally, the simulated and experimental results show that the proposed control strategy has better stability and decoupling performance than the decoupling control strategy based on the LS-SVM inverse system and PID (Proportion Integral Derivative).

1. INTRODUCTION

A permanent magnet synchronous generator has many advantages, such as simple structure, high efficiency, high power density, flexible topological structure, and reliable operation. It is widely used in many occasions such as wind turbines, gas turbine generators, aviation power supplies, and hybrid vehicles in [1–3]. Traditional generators use mechanical bearings to support the rotating shaft, which causes severe friction and wear as the speed increases. To solve this problem, outer rotor coreless bearingless permanent magnet synchronous generator (ORC-BPMSG) is proposed in [4–6]. Compared with the traditional permanent magnet synchronous generator, ORC-BPMSG has the advantages of high speed, high precision, no friction and wear. Because of the outer rotor and coreless structure, the ORC-BPMSG also has the advantages of no tooth groove torque, no core loss, and high moment of inertia. Therefore, ORC-BPMSG has a broad application prospect in wind turbine and flywheel energy storage system in [7, 8].

ORC-BPMSG is a nonlinear, strongly coupled, multivariate system. In order to obtain better dynamic and static performance, the study of its decoupling control is essential. Nowadays, inverse system theory is widely used in the decoupling control of nonlinear systems. In [9], the internal mode control strategy and inverse system are adopted to realize the nonlinear decoupling control of double-fed wind turbines. However, using the analytical method to obtain the inverse system relies too much on the mathematical model of the original system; the robustness of the system is poor; and the amount of calculation is large, which is not suitable for real-time control. In [10, 11], the neural network is

Received 21 October 2022, Accepted 14 December 2022, Scheduled 22 December 2022
* Corresponding author: Liangyu Shen (2222007109@stmail.ujs.edu.cn).
The authors are with the School of Electrical and Information Engineering, Jiangsu University, Zhenjiang 212013, China.

used to train the inverse system of the original system, thus realizing the decoupling control of the bearingless permanent magnet synchronous motor and improving the static and dynamic performance of the system. However, the neural network training inverse system has shortcomings such as local minima, slow learning speed, and long training time. In [12–14], the least square support vector machine (LS-SVM) is used to construct the inverse system of the original system, so as to realize decoupling control and make the system have good dynamic and static performance. The generalization ability of the LS-SVM is better than that of neural network, which greatly improves the training efficiency.

The traditional LS-SVM is an offline algorithm, and the nonlinear system model cannot be continuously updated through subsequent samples to achieve model correction, and the training is time-consuming, which is not suitable for real-time control of the system. In [15], an LS-SVM algorithm based on an improved weighting function is proposed, and the improved algorithm has better real-time performance and higher accuracy. In [16], an incremental support vector machine based on distance ratio and k-nearest neighbor is proposed, which improves the speed of the algorithm. In [17], the online least-squares support vector machine is proposed, and the online correlated vector machine models to capture the lag behavior, so that the lag model can be continuously updated with subsequent samples. In [18, 19], the parameters of LS-SVM are optimized by improved genetic algorithm (GA) and improved particle swarm optimization (PSO) to improve the performance of LS-SVM, thus improving the fitting accuracy of the inverse system. In [20], a differential evolution algorithm is developed to optimize the parameters and weights of the LS-SVM submodels to improve the generalization ability of the model, which ultimately improves the accuracy of the prediction model.

The OLS-SVM based on the rectangular window algorithm proposed in this paper is an online algorithm that realizes the real-time identification of the inverse system, thereby realizing the linearization and decoupling of ORC-BPMSG. In Section 2, the operation principle and mathematical model of the ORC-BPMSG are given. In Section 3, the real-time inverse system based on the OLS-SVM is introduced. In Section 4, the inverse system and original system are connected in series to form a pseudo-linear system, and the internal model controller is designed as the closed-loop controller of the system. In Section 5, the simulation results comparing the proposed control strategy with the control strategy based on the LS-SVM inverse system and PID are described. The experiments are conducted to verify theoretical analysis in Section 6, and conclusions are drawn in Section 7.

2. OPERATION PRINCIPLE AND MATHEMATICAL MODEL OF THE ORC-BPMSG

2.1. Operation Principle of the ORC-BPMSG

Compared with the structure of a traditional permanent magnet synchronous generator, there are two sets of windings in the stator of an ORC-BPMSG: the generation winding and suspension force winding. When the difference between the number of pole pairs P_B of the suspension force winding and the number of pole pairs P_G of the generation winding is 1, and the rotation direction and electrical angular velocity of the magnetic field generated by the suspension force winding and the generation winding are consistent, the condition of ORC-BPMSG rotor suspension is satisfied.

As shown in Fig. 1, the outer layer is the generation winding, $P_G = 3$. The inner layer is the suspension force winding, $P_B = 2$. The generation winding provides magnetic flux ψ_G. The suspension force winding is used to generate magnetic flux ψ_B. The prime mover drives the ORC-BPMSG to rotate, and the power generation winding cuts the magnetic field line to generate an induced current. When the suspension force winding N_B is not supplied with current, the magnetic flux ψ_G inside the air gap generated by the permanent magnet and generation winding current is evenly and symmetrically distributed, and no radial suspension force is generated. When the current shown in the Fig. 1 is passed into the suspension force winding, the flux linkage ψ_B generated by the suspension force winding current interacts with the original flux linkage; the magnetic field at the air gap 1 is increased; the magnetic field at the air gap 2 is weakened; and the radial suspension force F_x is produced in the x direction. By changing the direction of the current flowing in the suspension force winding, a controllable radial suspension force can be generated, so that the rotor of the ORC-BPMSG can be stably suspended.

In the power generation process of the ORC-BPMSG, there are situations such as variable speed and load, so pulse width modulation (PWM) rectifier is used to stabilize the voltage and constant

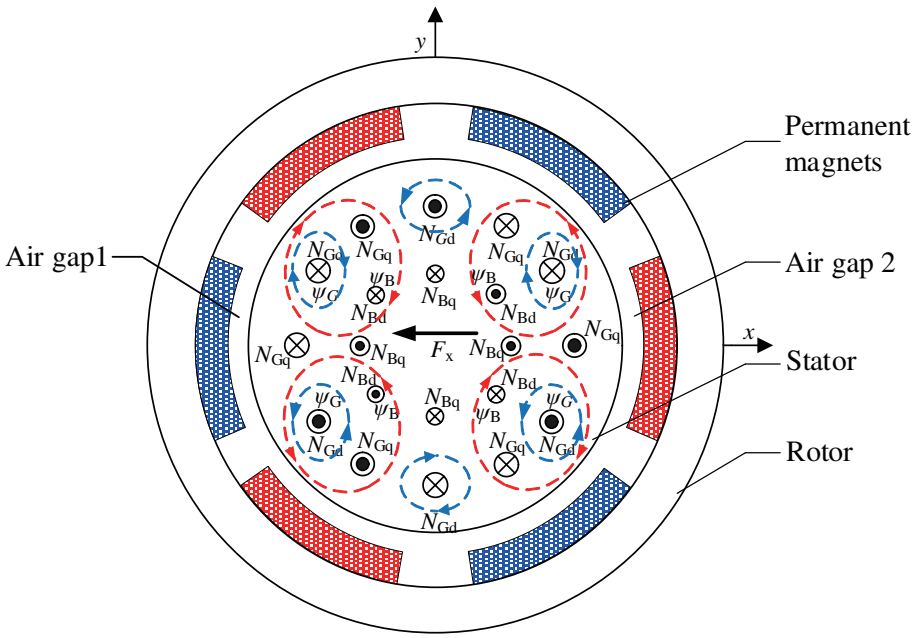

Figure 1. Schematic diagram of suspension force generation.

frequency. The PWM rectifier can convert the alternating current into direct current that is convenient for storage and conversion, which can improve the power factor of the AC side generator and reduce the harmonics of the generator current. The circuit diagram is shown in Fig. 2.

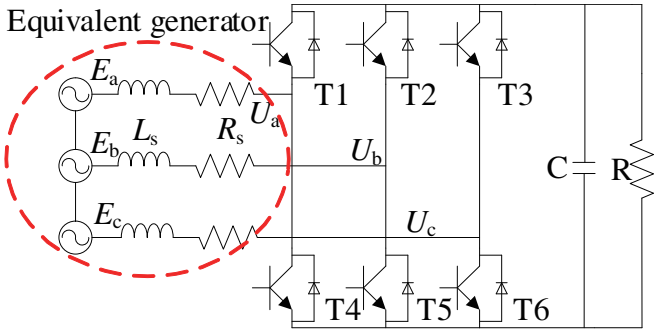

Figure 2. PWM rectifier circuit.

2.2. Mathematical Model

The three-phase magnetic chain equation for the ORC-BPMSG is expressed as:

$$\begin{cases} \psi_{\mathrm{a}} = -L_{\mathrm{a}} i_{\mathrm{a}} - M_{\mathrm{ab}} i_{\mathrm{b}} - M_{\mathrm{ac}} i_{\mathrm{c}} + \psi_{\mathrm{af}} \\ \psi_{\mathrm{b}} = -L_{\mathrm{b}} i_{\mathrm{b}} - M_{\mathrm{ba}} i_{\mathrm{a}} - M_{\mathrm{bc}} i_{\mathrm{c}} + \psi_{\mathrm{bf}} \\ \psi_{\mathrm{c}} = -L_{\mathrm{c}} i_{\mathrm{c}} - M_{\mathrm{ca}} i_{\mathrm{a}} - M_{\mathrm{cb}} i_{\mathrm{b}} + \psi_{\mathrm{cf}} \end{cases} \tag{1}$$

where ψ_a, ψ_b, ψ_c are three-phase stator magnetic chains. i_a, i_b, i_c are the induced current in the generation winding. L_a, L_b, L_c are the self-inductances of the power generation windings, respectively. M_{ab}, M_{ac}, M_{ba}, M_{bc}, M_{ca}, M_{cb} are the inductances between the generation windings. ψ_{af}, ψ_{bf}, ψ_{cf} are the magnetic chains produced by permanent magnet.

According to the magnetic chain equation, the voltage equation of the ORC-BPMSG can be expressed as:

$$\begin{cases} u_{sd} = R_s i_{sd} - \omega_r \psi_{sq} + \dfrac{d\psi_{sd}}{dt} \\ u_{sq} = R_s i_{sq} - \omega_r \psi_{sd} + \dfrac{d\psi_{sq}}{dt} \end{cases} \tag{2}$$

where u_{sd}, u_{sq} are the components of the output voltages in the d- and q-axes. R_s is the stator winding resistance. ω_r is the electric angular velocity. ψ_{sd}, ψ_{sq} are the components of the magnetic chains in the d and q-axes.

According to the Maxwell tensor method, the mathematical model of the radial suspension force of the ORC-BPMSG is established. The radial suspension force F_x and F_y in the x- and y-axes can be expressed as:

$$\begin{cases} F_x = (k_G - k_L)(i_{Bd}\psi_{Gd} + i_{Bq}\psi_{Gq}) + k_c x \\ F_{\mathrm{y}} = (k_G + k_L)(i_{Bq}\psi_{Gd} - i_{Bd}\psi_{Gq}) + k_c y \end{cases} \tag{3}$$

where i_{Bd} and i_{Bq} are the current components of the d- and q-axes of the suspension force winding, respectively. ψ_{Gd} and ψ_{Gq} are the equivalent air gap flux linkages of the permanent in the d- and q-axes of the generation winding, respectively. x and y are the offset in the x- and y-axes, respectively. k_G is the Maxwell force constant, k_L the Lorentz force constant, and k_c the offset constant.

It can be seen that the ORC-BPMSG is a multivariable, nonlinear and strongly coupled system.

2.3. Reversibility Analysis

According to the Newtonian equation of motion and the output voltage equation of the PWM rectifier, the following results are obtained.

$$\begin{cases} m\ddot{x} = F_{\mathrm{x}} - f_{\mathrm{x}} \\ m\ddot{y} = F_{\mathrm{y}} - f_{\mathrm{y}} \\ \dot{U}_{\mathrm{DC}} = \dfrac{3}{2C}(i_{\mathrm{Gq}} s_{\mathrm{q}} + i_{\mathrm{Gd}} s_{\mathrm{d}}) - \dfrac{1}{C} i_{\mathrm{L}} \end{cases} \tag{4}$$

where m is the mass of the rotor. f_x and f_y are the interference force in the x- and y-axes, respectively. U_{DC} is the voltage output of PWM rectifier. C is the capacitance of PWM rectifier. s_d and s_q are the switching functions in the d- and q-axes, respectively. i_L is the load current of PWM rectifier.

The status variable X, input variable $\boldsymbol{U}$, and output variable $\boldsymbol{Y}$ of the system can be set as:

$$\begin{cases} \mathbf{X} = [x_1, x_2, x_3, x_4, x_5]^{\mathrm{T}} = [x, y, \dot{x}, \dot{y}, U_{\mathrm{DC}}]^{\mathrm{T}} \\ \mathbf{U} = [u_1, u_2, u_3, u_4]^{\mathrm{T}} = [i_{\mathrm{Gd}}, i_{\mathrm{Gq}}, i_{\mathrm{Bd}}, i_{\mathrm{Bq}}]^{\mathrm{T}} \\ \mathbf{Y} = [y_1, y_2, y_3]^{\mathrm{T}} = [x, y, U_{\mathrm{DC}}]^{\mathrm{T}} \end{cases} \tag{5}$$

It can be seen from Equation (6) that each component of the output variable $\boldsymbol{Y}$ is derived until the input variable $\boldsymbol{U}$ is explicitly included in the derivation expression.

$$\begin{cases} \dot{y}_1 = \dot{x}_1 = x_3 \\ \ddot{y}_1 = \ddot{x}_1 = \dot{x}_3 = K(L_{\mathrm{Gd}} u_1 u_3 + L_{Gq} u_2 u_4 + \psi_f u_3)/m + k_c x_1/m - f_x/m \\ \dot{y}_2 = \dot{x}_2 = x_4 \\ \ddot{y}_2 = \ddot{x}_2 = \dot{x}_4 = K(L_{\mathrm{Gd}} u_1 u_4 - L_{\mathrm{Gq}} u_2 u_3 + \psi_f u_4)/m + k_c x_2/m - f_y/m \\ \dot{y}_3 = \dot{x}_5 = {}^{3}\!/_{2C}\,(S_{\mathrm{d}} u_1 + S_{\mathrm{q}} u_2) - {}^{1}\!/_{C} i_L \end{cases} \tag{6}$$

According to Equation (6), the Jacobi matrix shown in Equation (7) can be obtained.

$$\mathbf{A} = \left[\frac{\partial(\ddot{y}_1, \ddot{y}_2, \dot{y}_3)}{\partial \mathbf{U}}\right] = \frac{K}{m} \cdot \begin{bmatrix} L_{\mathrm{Gd}} u_3 & L_{\mathrm{Gq}} u_4 & L_{\mathrm{Gd}} u_1 + \psi_f & L_{\mathrm{Gq}} u_2 \\ L_{\mathrm{Gd}} u_4 & -L_{\mathrm{Gq}} u_3 & -L_{\mathrm{Gq}} u_2 & L_{\mathrm{Gd}} u_1 + \psi_f \\ {}^{3}\!/_{2C} S_{\mathrm{d}} & {}^{3}\!/_{2C} S_{\mathrm{q}} & 0 & 0 \end{bmatrix} \tag{7}$$

The rank of the Jacobi matrix is 3, and its relative order is $\alpha = (\alpha_1,\ \alpha_2,\ \alpha_3) = (2, 2, 1)$, which satisfies $\alpha_1 + \alpha_2 + \alpha_3 \leq 5$ (5 is the number of state variables). It can be seen that the original system is reversible, and the expression of the inverse system function is shown in Equation (8).

$$\mathbf{U} = [u_1, u_2, u_3, u_4]^{\mathrm{T}} = \xi(\mathbf{X}, \ddot{y}_1, \ddot{y}_2, \dot{y}_3) \tag{8}$$

3. OLS-SVM ALGORITHM

3.1. LS-SVM Algorithm

LS-SVM is an important method to realize the decoupling control based on the inverse system theory. LS-SVM uses the least-squares linear system as a loss function, instead of the traditional quadratic programming method. For the training sample $\{\mathbf{x}_k, \mathbf{y}_k\}_{k=1}^{l}$, $k = 1, 2, \ldots, l$, $\boldsymbol{x}_k$ and $\boldsymbol{y}_k$ are the inputs and the output, respectively. The input space is mapped to the high-dimensional feature space by the nonlinear mapping $\varphi(x)$, using the linear function of the high-dimensional feature space as shown in formula (9).

$$\mathbf{y} = \boldsymbol{\omega}^{\mathrm{T}}\boldsymbol{\varphi}(\mathbf{x}) + \mathbf{b} \tag{9}$$

Using formula (9) to fit the sample, ω is the weight vector to determine the feature space, and $\boldsymbol{b}$ is the bias. The optimization problem for the LS-SVM is defined as:

$$\min \mathbf{J}(\boldsymbol{\omega},\mathbf{e}) = \frac{1}{2}\boldsymbol{\omega}^{\mathrm{T}}\boldsymbol{\omega} + \frac{1}{2}\gamma \sum_{\mathrm{i}=1}^{\mathrm{n}} \mathbf{e}_{\mathrm{i}}^2 \tag{10}$$

where γ is the penalty factor. $\boldsymbol{e}_i$ is the relaxation factor. n is the number of training samples.

The constraint can be expressed as follows.

$$\mathbf{y}_k = \boldsymbol{\omega}^{\mathrm{T}}\boldsymbol{\varphi}(x) + \mathbf{b} + \mathbf{e}_i, \quad i = 1, \ldots, n \tag{11}$$

The above optimization problem is solved by the Lagrange method, and the Lagrange function is obtained.

$$L(\boldsymbol{\omega}, \mathbf{b}, \mathbf{e}, \alpha) = \mathbf{J}(\boldsymbol{\omega}, \mathbf{e}) - \sum_{i=1}^{n} \alpha_i \left[\boldsymbol{\omega}^{\mathrm{T}}\boldsymbol{\varphi}(\mathbf{x}_i) + \mathbf{b} + \mathbf{e}_i - \mathbf{y}_i\right] \tag{12}$$

where α_i is a Lagrange multiplier.

The analytical solution of the suboptimization problem is obtained by the Karush-Kuhn-Tucker (KKT) optimal condition.

$$\begin{bmatrix} 0 & \mathbf{I}^{\mathrm{T}} \\ \mathbf{I} & \boldsymbol{\Omega} + \gamma^{-1}\mathbf{I} \end{bmatrix} \begin{bmatrix} \mathbf{b} \\ \alpha \end{bmatrix} = \begin{bmatrix} 0 \\ \mathbf{y} \end{bmatrix} \tag{13}$$

where $\boldsymbol{y} = [\boldsymbol{y}_1, \ldots, \boldsymbol{y}_n]^T$. $\boldsymbol{I}$ is the unit matrix. $\Omega = K(\boldsymbol{x}_i,\ \boldsymbol{x}_j)$. $K(\boldsymbol{x}_i,\ \boldsymbol{x}_j)$ is the kernel meeting the Mercer condition, and the Gaussian kernel function is used in this paper.

The inverse system regression equation is as follows.

$$\mathbf{y}(x) = \sum_{i=1}^{n} \alpha_i K(\mathbf{x}, \mathbf{x}_i) + \mathbf{b} \tag{14}$$

where $K(\mathbf{x}, \mathbf{x}_k) = \exp(\frac{-||\mathbf{x}-\mathbf{x}_k||^2}{2\sigma^2})$ is the Gaussian kernel function, and σ is the kernel width.

3.2. OLS-SVM Algorithm

In this paper, the standard LS-SVM algorithm is combined with the rectangular window algorithm to study the OLS-SVM based on the rectangular window algorithm. The estimates of the rectangular window algorithm rely only on a finite number of past data, and all old data were completely removed. Thus, the samples of the OLS-SVM algorithm scroll over time. When a new sample comes in, an old sample is discarded, and the number of samples remains constant. However, the rectangular window algorithm simply discards the old data and does not consider the influence of the old data, so the

forgetting factor β is introduced to process the old data in this paper. Therefore, the proposed algorithm considers both the influence of the old data and the effect of the new data.

Suppose that the rectangular window width is m. For the given set of training samples $\{(\mathbf{x}_i, \mathbf{y}_i), \mathbf{x}_i \in R^n, \mathbf{y}_i \in R^n\}$, the training samples at time k are $(\boldsymbol{X}_k,\ \boldsymbol{Y}_k)$, where $\mathbf{X}_k = [\mathbf{x}_{k-m-1}, \ldots, \mathbf{x}_k]$, $\mathbf{Y}_k = [\mathbf{y}_{k-m-1}, \ldots, \mathbf{y}_k]$. The kernel function matrix Ω, the Lagrange multiplier α, and the bias to be calculated can be expressed as:

$$\begin{cases} \boldsymbol{\Omega}_k(i,j) = K(\mathbf{x}_{k-m+i}, \mathbf{x}_{k-m+j}) \\ \alpha(k) = [\ \alpha_{k-m+1} \quad \alpha_{k-m+2} \quad \cdots \quad \alpha_{k-m}\ ] \\ \mathbf{b}(k) = \mathbf{b}_k \end{cases} \tag{15}$$

Let $\mathbf{Q}_k = \boldsymbol{\Omega}_k + \mathbf{I}/\gamma$, then:

$$\begin{bmatrix} 0 & \mathbf{I}^T \\ \mathbf{I} & \mathbf{Q}_k \end{bmatrix} \begin{bmatrix} \mathbf{b}(k) \\ \alpha(k) \end{bmatrix} = \begin{bmatrix} 0 \\ \mathbf{y}_k \end{bmatrix} \tag{16}$$

Let $\boldsymbol{\theta}_k = \begin{bmatrix} \mathbf{b}(k) \\ \alpha(k) \end{bmatrix}$, $\boldsymbol{\Phi}_k = \begin{bmatrix} 0 & \mathbf{I}^T \\ \mathbf{I} & \mathbf{Q}_k \end{bmatrix}$, $\mathbf{z}_k = \begin{bmatrix} 0 \\ \mathbf{y}_k \end{bmatrix}$, then:

$$\boldsymbol{\Phi}_k \boldsymbol{\theta}_k = \mathbf{z}_k \tag{17}$$

The linear recursive algorithm can be used to adjust the OLS-SVM model parameters in real time, then:

$$\begin{cases} \boldsymbol{\theta}_{k+1} = \boldsymbol{\theta}_k + \mathbf{N}_{k+1}(\mathbf{z}_{k+1} - \boldsymbol{\Phi}_{k+1}\boldsymbol{\theta}_k) \\ \mathbf{N}_{k+1} = \mathbf{M}_k \boldsymbol{\Phi}_{k+1}(\beta \mathbf{I} + \boldsymbol{\Phi}_{k+1}\mathbf{M}_k\boldsymbol{\Phi}_{k+1})^{-1} \\ \mathbf{M}_{k+1} = \dfrac{1}{\beta}[\mathbf{M}_k - \mathbf{N}_{k+1}\boldsymbol{\Phi}_{k+1}\mathbf{M}_k] \\ \mathbf{M}_0 = \lambda^2 \mathbf{I} \end{cases} \tag{18}$$

The training flowchart of the ORC-BPMSG inverse system based on the OLS-SVM algorithm is shown in Fig. 3.

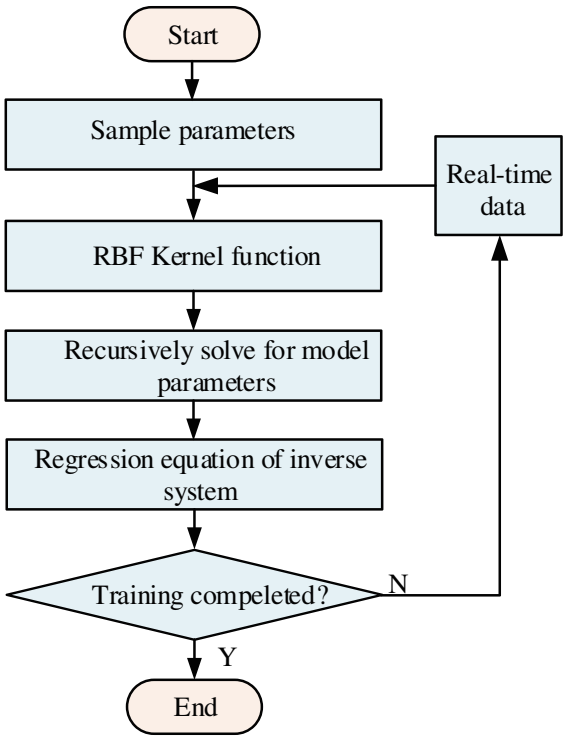

Figure 3. Inverse system training flow chart.

4. DESIGN OF ADDITIONAL CLOSED-LOOP CONTROLLERS

The inverse system of the ORC-BPMSG trained by OLS-SVM is connected in series with the original system to construct a pseudo-linear system as shown in Fig. 4. The ORC-BPMSG is decoupled into a voltage first-order pseudo-linear subsystem and two displacement second-order pseudo-linear subsystems.

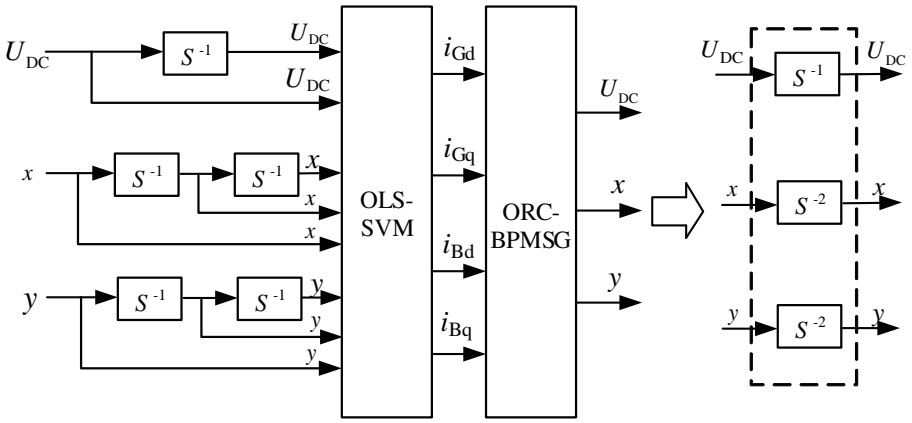

Figure 4. Pseudo linear system.

The pseudo-linear system is an open-loop system. In order to obtain better dynamic performance, an additional closed-loop controller needs to be designed to realize the closed-loop control of the controlled object. In this paper, the internal model controller is designed to perform closed-loop control, and the block diagram of the internal model controller is shown in Fig. 5.

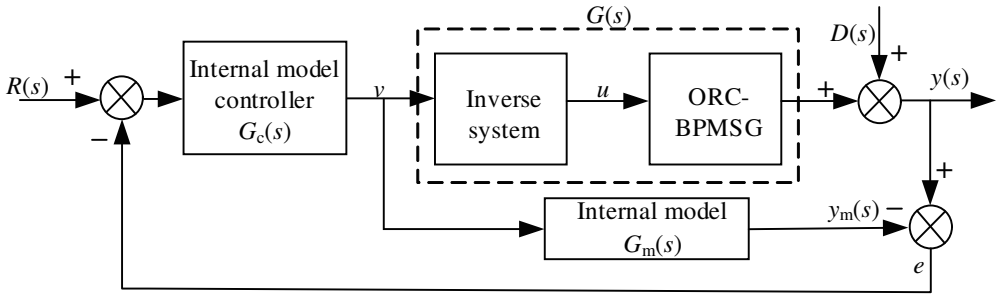

Figure 5. Block diagram of the internal model controller.

The internal model of the ORC-BPMSG is:

$$G_{\mathrm{m}}(s) = \begin{bmatrix} \dfrac{1}{s} & 0 & 0 \\ 0 & \dfrac{1}{s^2} & 0 \\ 0 & 0 & \dfrac{1}{s^2} \end{bmatrix} \tag{19}$$

Because $G_m(s)$ is a steady-state transfer function, the internal model controller $G_c(s)$ is:

$$G_c(s) = F(s)G_{\mathrm{m}}(s)^{-1} \tag{20}$$

Due to the errors in the actual system and theoretical modeling, $G(s) \neq G_{\mathrm{m}}(s)$. According to the multiplicative uncertainty of the transfer function, the pseudo linear system can be assumed as:

$$G(s) = G_{\mathrm{m}}(s)(1 + l_{\mathrm{m}}(s)) \tag{21}$$

In order to reduce the sensitivity of the modeling error of the internal model control system and improve the robust stability of the ORC-BPMSG closed-loop system, a low-pass filter $F(s)$ is introduced as

$$F(s) = \frac{1}{(\lambda s + 1)^n} \tag{22}$$

where λ is the system time constant, and n is the system order.

Then the error of the closed-loop system is:

$$E(s) = \frac{1 - G_c(s)G_{\mathrm{m}}(s)}{1 + G_{\mathrm{c}}(s)[G(s) - G_{\mathrm{m}}(s)]}[R(s) - D(s)] \tag{23}$$

When $D(s) = 0$, and the input is a step signal, the error of the system is:

$$e(\infty) = \lim_{s \to 0} \frac{1 - F(s)}{1 + F(s)l_m(s)} \frac{r_0}{s} = 0 \tag{24}$$

When $R(s) = 0$, and the disturbance is a constant value, the error of the system is:

$$e(\infty) = \lim_{s \to 0} \frac{1 - F(s)}{1 + F(s)l_m(s)}[-D(s)] = 0 \tag{25}$$

It can be seen from the above formulas that by using the internal model control structure to control the obtained pseudo-linear system, the step signal can be tracked without static error, and the constant value disturbance can be completely suppressed.

The decoupling control block diagram of the ORC-BPMSG based on the OLS-SVM inverse system and internal model controllers is shown in Fig. 6.

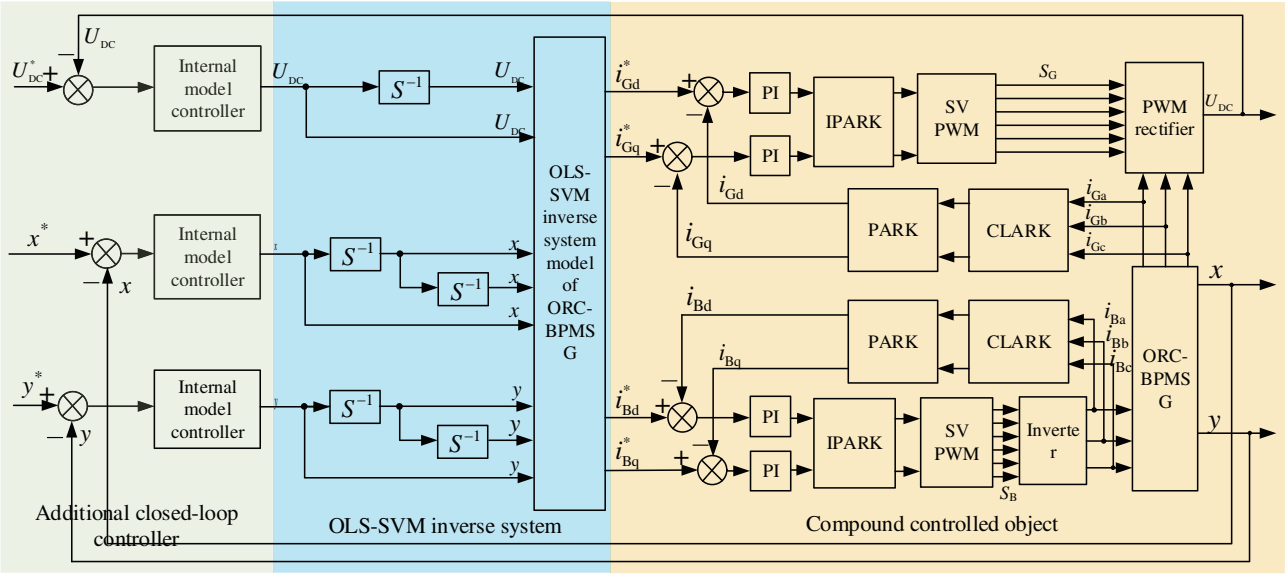

Figure 6. Block diagram of decoupling control based on the OLS-SVM inverse system and internal model controllers of the ORC-BPMSG.

5. SIMULATION TEST

The simulation is carried out in MATLAB, and the relevant parameters are as follows. The parameter of the internal model controller for the voltage subsystem $\lambda = 0.05$; the parameter of the internal model controller for the displacement subsystem $\lambda = 0.03$. The parameter of the PI controller for the voltage subsystem $K_p = 3.75$, $K_i = 469$; the parameter of the PID controller for the displacement subsystem $K_p = 50$, $K_i = 357$, $K_d = 7.5$.

In order to compare the predictive ability of the OLS-SVM algorithm and LS-SVM algorithm, the relative error of the model predicted value and the actual measured value is set as follows:

$$E = \left| \frac{y_i - \hat{y}_i}{y_i} \right| \times 100\% \tag{26}$$

Figure 7 is the relative error curve of displacement prediction of OLS-SVM algorithm and LS-SVM algorithm. Comparing the two curves in the figure, it can be seen that the relative error value of the prediction of the OLS-SVM algorithm is much smaller than that of the LS-SVM algorithm, and its relative error value is about 0 near the equilibrium position. It can be seen that the prediction ability of the OLS-SVM algorithm is stronger than that of the LS-SVM algorithm.

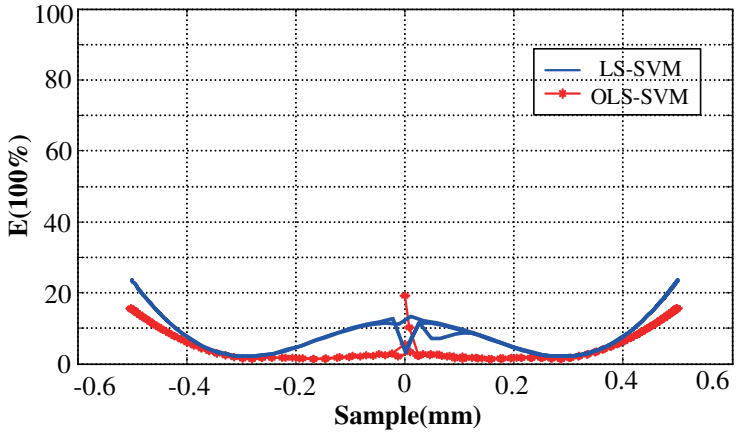

Figure 7. Relative error curve of displacement prediction of OLS-SVM algorithm and LS-SVM algorithm.

In order to verify that the proposed control strategy can better realize the decoupling control between the output voltage and the suspension force of the ORC-BPMSG, the decoupling simulation curve between the output voltage and suspension force is shown in Fig. 8. At 0.3 s, the given voltage is increased from 220 V to 280 V. When the decoupling control strategy based on the LS-SVM inverse system and PID is adopted, the overshoot of the output voltage is 3.57%, and the adjustment time is 0.06 s. Due to the coupling relationship between the output voltage and suspension force, a disturbance with an amplitude of 20 µm is generated in the x direction, and the adjustment time is 0.04 s. A disturbance with an amplitude of 18 µm is generated in the y direction, and the adjustment time is 0.03 s. When the control strategy proposed in this paper is adopted, the output voltage has almost no overshoot, and the adjustment time is 0.02 s. The radial displacement in the x- and y-directions is hardly disturbed. It can be concluded that the proposed control method has better tracking performance and stability when a given voltage is abruptly changed, and better realizes the decoupling control between the output voltage and the suspension force.

In order to verify that the proposed control strategy can realize the decoupling control between the suspension forces of the ORC-BPMSG, the decoupling simulation curve between the suspension forces is shown in Fig. 9. At 0.1 s–0.2 s, a pulse with an amplitude of 200 µm is applied in the x direction. When the decoupling control strategy based on the LS-SVM inverse system and PID is adopted, the radial displacement in the x direction has an overshoot of 10 µm at the beginning of the pulse, and the adjustment time is 0.01 s. Due to the coupling between the suspension forces, a disturbance with an amplitude of 10 µm is generated in the y direction, and the adjustment time is 0.01 s. At the end of the pulse, the radial displacement in the x direction has a disturbance of 16 µm, and the adjustment time is 0.02 s. Due to the coupling between the suspension forces, the disturbance in the y direction with an amplitude of 18 µm is generated, and the adjustment time is 0.01 s. When the control strategy proposed in this paper is adopted, the radial displacement in the x direction does not overshoot at the beginning of the pulse, which has little effect on the radial displacement in the y direction. At the end of the

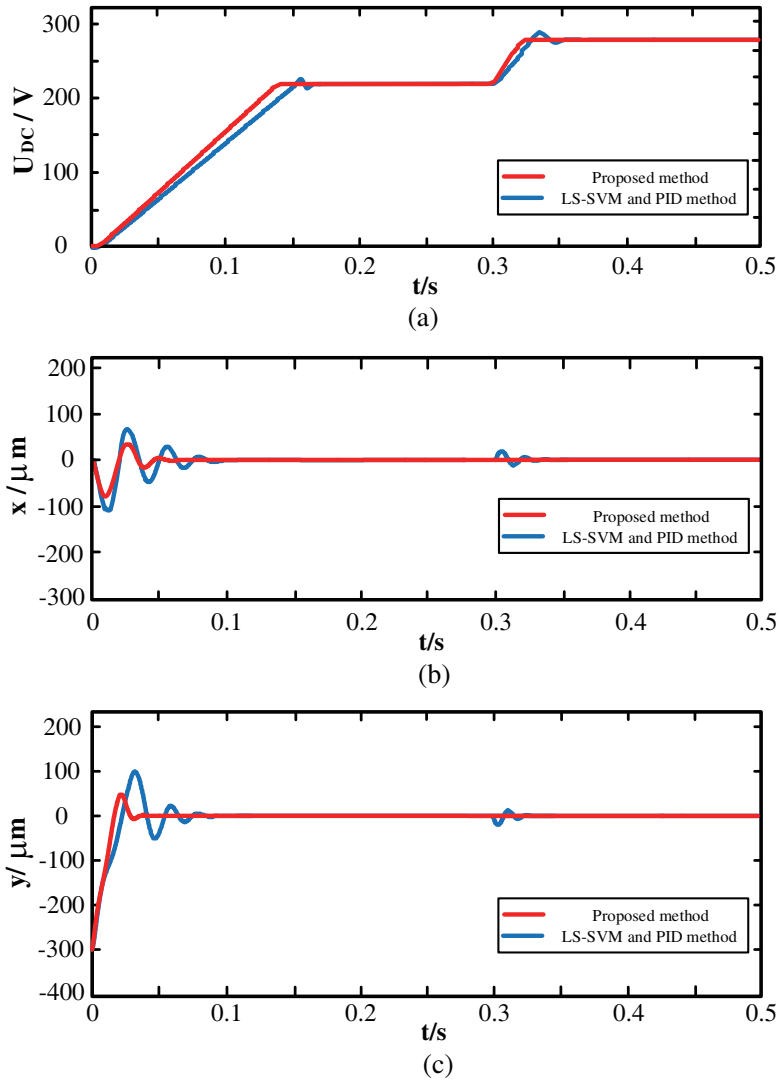

Figure 8. Decoupling simulation curve of output voltage and suspension force of the ORC-BPMSG. (a) Output voltage, (b) displacement in the x direction, (c) displacement in the y direction.

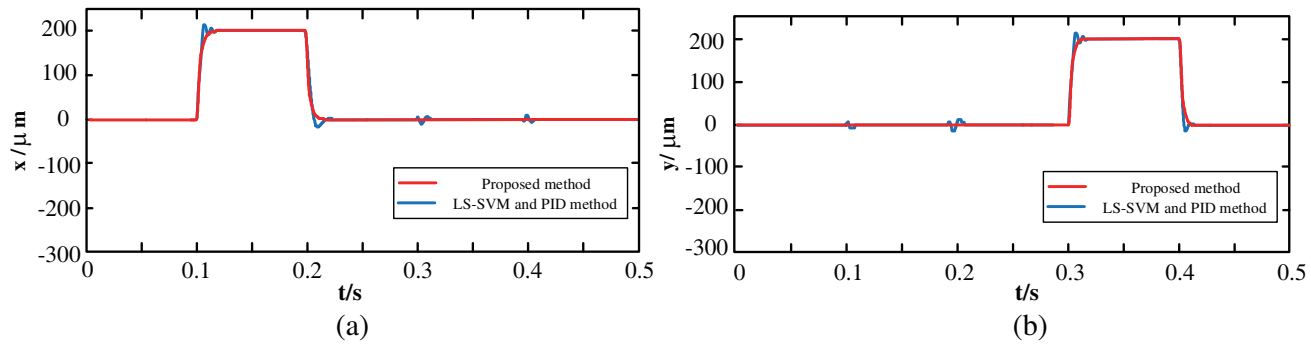

Figure 9. Decoupling simulation curve of suspension forces of the ORC-BPMSG. (a) Displacement in the x direction, (b) displacement in the y direction.

pulse, the radial displacement in the x direction has no overshoot, which has little effect on the radial displacement in the y direction. Similar results were obtained by applying a pulse with an amplitude of 200 µm in the y direction at 0.3 s–0.4 s. It can be concluded that the proposed control method can better realize the decoupling control between the suspension forces.

In order to verify that the proposed control strategy makes the ORC-BPMSG more resistant to interference, the displacement simulation curve of anti-interference of the ORC-BPMSG is shown in Fig. 10. At 0.2 s, a 30 N interference force is applied in the y direction. When using the decoupling control strategy based on the LS-SVM inverse system and PID, the radial displacement in the y direction produces a disturbance of 67 µm, and the adjustment time is 0.06 s. When the proposed decoupling control strategy is adopted, the radial displacement in the y direction produces a disturbance of 33 µm, and the adjustment time is 0.04 s. It can be concluded that the proposed control method has stronger anti-interference ability than the decoupling control strategy based on the LS-SVM inverse system and PID.

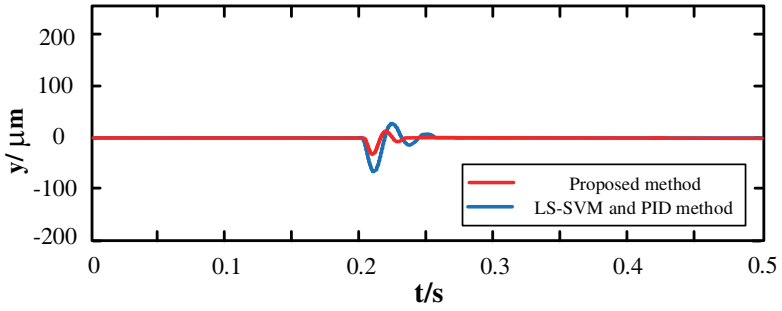

Figure 10. Displacement simulation curve of anti-interference of the ORC-BPMSG.

It can be seen from the above data analysis that since the LS-SVM algorithm is an offline algorithm, the fitting accuracy is limited, and it is difficult to achieve high-performance control by using the PID controller as an additional closed-loop controller, so the system still has slight coupling. The OLS-SVM proposed in this paper is an online algorithm, which can realize the identification and correction of the ORC-BPMSG inverse system, making the fitting of the inverse system more accurate. The internal model controller is used as an additional closed-loop controller, which improves the tracking and anti-interference performance of the system, and improves the decoupling performance and stability of the system.

6. EXPERIMENT RESEARCH

6.1. Experimental Platform and Prototype Parameters

In order to verify the effectiveness of the decoupling control strategy based on the OLS-SVM inverse system and internal model controllers, the ORC-BPMSG which has 3 pole pairs of generation winding and 2 pole pairs of suspension winding is used as the control object for experimental research. The relevant parameters are shown in Table 1. The experiment uses DSP TMS320F28335 as the core digital controller, and the experimental platform is shown in Fig. 11.

6.2. Dynamic Decoupling Experiment

Figure 12 is the decoupling experimental curve of the output voltage and suspension force of the ORC-BPMSG. The proposed control method is adopted as shown in Fig. 12(a). When the given voltage is raised from 200 V to 280 V, there is no overshoot phenomenon, and the response time is about 0.15 s. When the voltage is changed, the radial displacement in the x direction produces a disturbance of 25 µm, and the radial displacement in the y direction produces a disturbance of 37 µm. The decoupling control strategy based on the LS-SVM inverse system and PID is adopted as shown in Fig. 12(b). When the given voltage is raised from 200 V to 280 V, there is an overshoot of 25 V, and the response time is

Table 1. Parameters of the prototype machine.

Symbol	Value	Symbol	Value
U_N (V)	220	δ (mm)	2
P_N (kW)	2	Ψ_f (Wb)	0.165
P_G	3	L_{Md} (mH)	13.42
P_B	2	L_{Mq} (mH)	13.42
m (kg)	2	L_{M2} (mH)	2.37

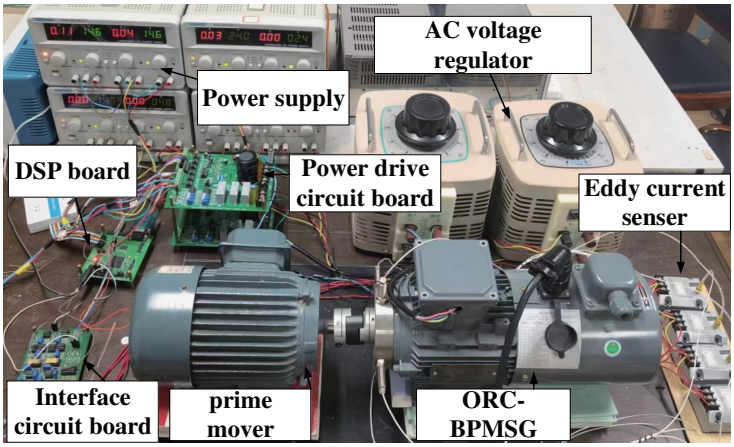

Figure 11. ORC-BPMSG experimental platform.

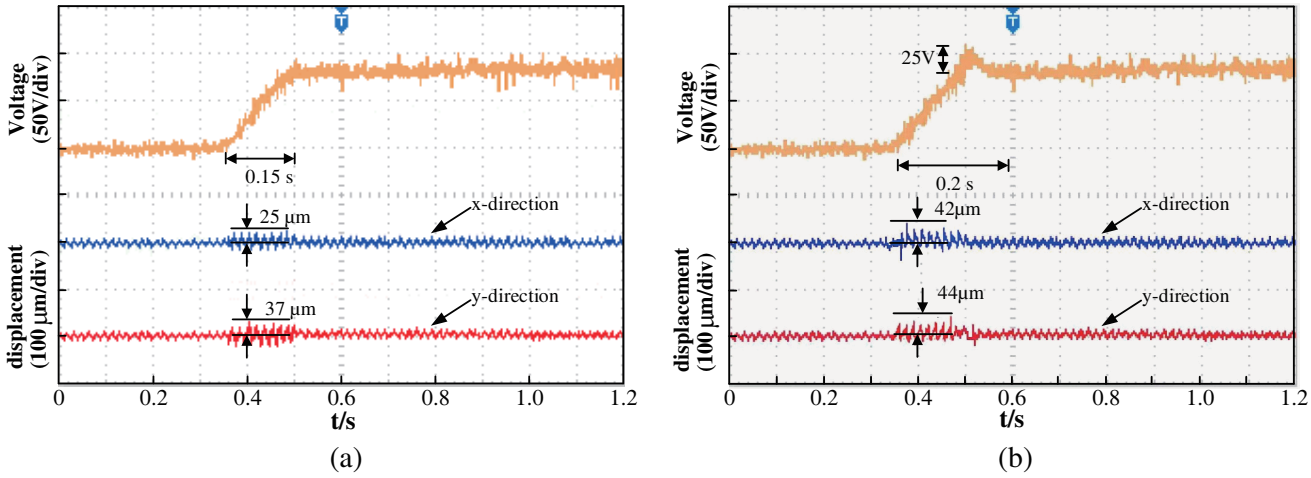

Figure 12. Decoupling experimental curve of output voltage and suspension force of the ORC-BPMSG. (a) Proposed method, (b) LS-SVM and PID method.

raised to about 0.2 s. In the process of voltage rise, the radial displacement in the x direction produces a disturbance of 42 μm, and the radial displacement in the y direction produces a disturbance of 44 μm. It is verified that the proposed control strategy has better tracking performance, stability, and decoupling performance of output voltage and suspension force.

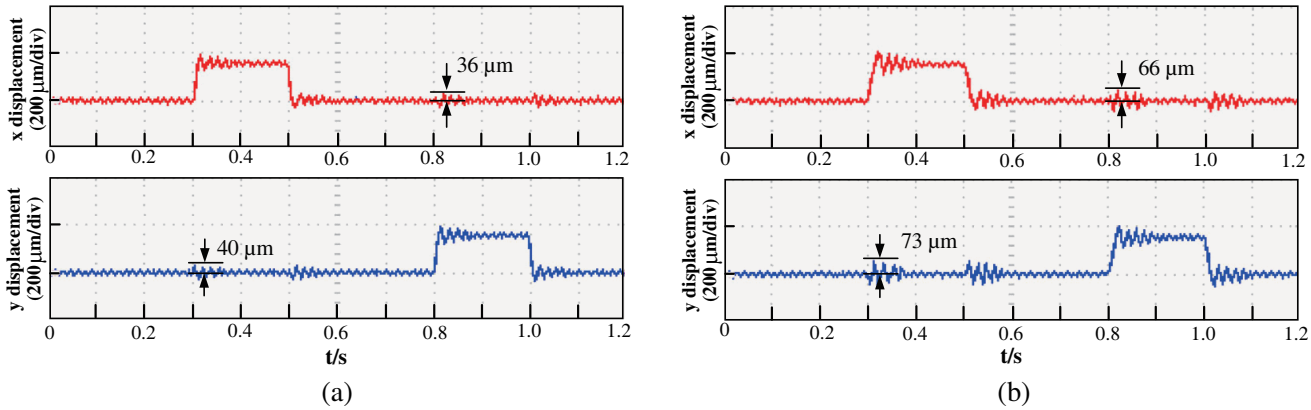

Figure 13. Decoupling experimental curve of suspension forces of the ORC-BPMSG. (a) Proposed method, (b) LS-SVM and PID method.

6.3. Static Decoupling Experiment

Figure 13 is the decoupling experimental curve of the decoupling of suspension forces of the ORC-BPMSG. The proposed decoupling control strategy is adopted as shown in Fig. 13(a). At 0.3 s, the displacement signal in the x direction is from 0 μm to 200 μm, and the radial displacement in the y direction produces a disturbance of 40 μm. At 0.8 s, the displacement signal in the y direction changes from 0 μm to 200 μm, and the radial displacement in the x direction produces a disturbance of 36 μm. The decoupling control strategy based on the LS-SVM inverse system and PID is adopted as shown in Fig. 13(b). At 0.3 s, the displacement signal in the x direction is from 0 μm to 200 μm, and the radial displacement in the y direction produces a perturbation of 73 μm. At 0.8 s, the displacement signal in the y direction changes from 0 μm to 200 μm, and the radial displacement in the x direction produces a perturbation of 66 μm. It is verified that the proposed control strategy has better decoupling performance for the suspension forces of the ORC-BPMSG.

6.4. Static Decoupling Experiment

Figure 14 is the anti-interference experimental curve of the ORC-BPMSG. The proposed decoupling control strategy is adopted as shown in Fig. 14(a). At 0.4 s, the interference force of 30 N is applied in the y direction, and the radial displacement in the y direction produces a disturbance of 87 μm, which returns to the equilibrium position after 0.1 s. The decoupling control strategy based on the LS-SVM inverse system and PID is adopted as shown in Fig. 14(b). At 0.4 s, the interference force of 30 N is applied in the y direction, and the radial displacement in the y direction produces a disturbance of

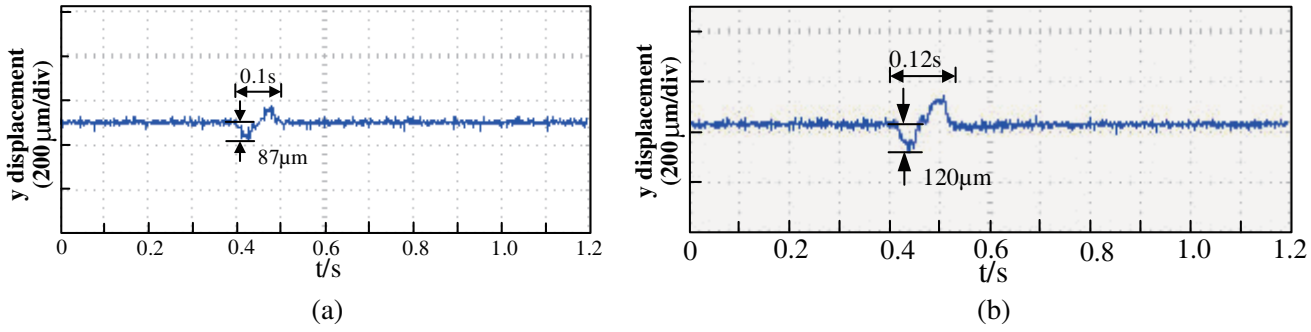

Figure 14. Anti-interference experimental curve of ORC-BPMSG. (a) Proposed method, (b) LS-SVM and PID method.

120 μm, which returns to the equilibrium position after 0.12 s. It is verified that the proposed control strategy has stronger anti-interference ability than the decoupling control strategy based on the LS-SVM inverse system and PID.

7. CONCLUSION

Aiming at the nonlinear, multi-variable, and strong coupling characteristics of the ORC-BPMSG, a decoupling control strategy based on the OLS-SVM inverse system and internal model controller is proposed. The inverse system is constructed by OLS-SVM, and a pseudo-linear system is formed in series with the original system, so as to realize linearization and decoupling. Through simulation and experimental research, the conclusions are as follows:

1) The OLS-SVM is an online algorithm, which can realize the identification and correction of the ORC-BPMSG inverse system, making the fitting of the inverse system more accurate. Therefore, the proposed method has better decoupling performance.
2) The internal model controller is designed as an additional closed-loop controller, which improves the tracking performance and anti-interference of the system.

ACKNOWLEDGMENT

This work was sponsored in part by the National Natural Science Foundation of China (61973144, 62273168).

REFERENCES

1. Xu, Q., S. Yuan, and X. Liu, "Online detection and location of eccentricity fault in PMSG with external magnetic sensing," *IEEE Transactions on Industrial Electronics*, Vol. 69, No. 10, 9749–9760, 2022.
2. Zhang, X., Y. Li, and K. Wang, "Model predictive control of the open-winding PMSG system based on three-dimensional reference voltage-vector," *IEEE Transactions on Industrial Electronics*, Vol. 67, No. 8, 6312–6322, 2020.
3. Nian, H. and L. Chen, "Control techniques of open winding PMSG systems fed by integration of three level NPC converters and diode bridges," *Chinese Society for Electrical Engineering*, Vol. 36, No. 22, 6238–6245, 2016.
4. Koczara, W. and E. Emest, "Smart and decoupled power electronic generation system," *Proceeding of IEEE Power Electronics Specialists Conference*, 1902–1907, 2004.
5. Ooshima, M., S. Kitazawa, A. Chiba, et al., "Design and analyses of a coreless-stator-type bearingless motor/generator for clean energy generation and storage systems," *IEEE Transactions on Magnetics*, Vol. 42, No. 10, 3461–3463, 2006.
6. Ooshima, M., S. Kobayashi, and H. Tanaka, "Magnetic suspension performance of a bearingless motor/generator for flywheel energy storage systems," *Proceeding of IEEE PES General Meeting*, 1–4, 2010.
7. Diao, X., Y. Hu, H. Zhu, et al., "Bearingless permanent magnet synchronous generator levitation force and electricity generation performance under variable speed and load situation," *Journal of Electrical Machinery and Control*, Vol. 21, No. 9, 63–72, 2017.
8. Hua, Y., H. Zhu, and Y. Xu, "Multi-objective optimization design of bearingless permanent magnet synchronous generator," *IEEE Transactions on Applied Superconductivity*. Vol. 30, No. 4, 1–5, 2020.
9. Liu, B., Y. Zhang, and X. Yan, "Internal model control of doubly fed induction generators based on inverse system method," *Power System Technology*, Vol. 35, No. 4, 149–153, 2011.
10. Sun, X., L. Chen, H. Jiang, et al., "High-performance control for a bearingless permanent-magnet synchronous motor using neural network inverse scheme plus internal model controllers," *IEEE Transactions on Industrial Electronics*, Vol. 6, No. 63, 3479–3488, 2016.

11. Gu, Z. and H. Zhu, "Active disturbance rejection control of 5-degree-of freedom bearingless permanent magnet synchronous motor based on fuzzy neural network inverse system." *ISA Transactions*, Vol. 101, 1–14, 2020.
12. Zhu, H., L. Cao, Y. Li, et al., "Decoupling control of 5-degree of freedom bearingless synchronous reluctance motor based on least square support vector machine inverse system," *Chinese Society for Electrical Engineering*, Vol. 33, No. 15, 99–108, 2013.
13. Liu, G., Y. Zhang, H. Wei, et al., "Least squares support vector machines inverse control for two-motor variable frequency speed-regulating system based on active disturbances rejection," *Chinese Society for Electrical Engineering*, Vol. 32, No. 6, 138–144, 2012.
14. Liu, G., L. Chen, W. Zhao, et al., "Internal model control of permanent magnet synchronous motor using support vector machine generalized inverse," *IEEE Transactions on Industrial Informatics*, Vol. 9, No. 2, 890–899, 2013.
15. Xing, J., R. Wang, Q. Yang, et al., "Online training algorithm research based on improved weighed LSSVM," *Proceeding of Chinese Control Conference*, 5055–5060, 2010.
16. Liu, B. and X. Cheng, "An incremental algorithm of support vector machine based on distance and K nearest neighbor," *Proceeding of IEEE International Conference on Computer Science and Automation Engineering*, 18–20, 2011.
17. Wong, P., Q. Xu, C. Vong, et al., "Rate-dependent hysteresis modeling and control of a piezo stage using online support vector machine and relevance vector machine," *IEEE Transactions on Industrial Electronics*, Vol. 59, No. 4, 1988–2001, 2011.
18. Xu, B. and H. Zhu, "The parameters of LS-SVM are optimized by improved genetic algorithm and improved particle swarm optimization algorithm to improve the performance of LS-SVM, thus improving the fitting accuracy of the inverse system," *IEEE Transactions on Industrial Electronics*, Vol. 69, No. 12, 12182–12190, 2022.
19. Zhu, H. and T. Liu, "Rotor displacement self-sensing modeling of six-pole radial hybrid magnetic bearing using improved particle swarm optimization support vector machine," *IEEE Transactions on Industrial Electronics*, Vol. 35, No. 11, 12296–12306, 2020.
20. Hu, J., M. Wu, X. Chen, et al., "A multilevel prediction model of carbon efficiency based on the differential evolution algorithm for the iron ore sintering process," *IEEE Transactions on Industrial Electronics*, Vol. 65, No. 11, 8778–8787, 2018.